High-Frame-Rate Echocardiography Using Coherent Compounding With Doppler-Based Motion-Compensation

Jonathan Porée, Daniel Posada, Amir Hodzic, François Tournoux, Guy Cloutier, and Damien Garcia*

***Abstract*—High-frame-rate ultrasonography based on coherent compounding of unfocused beams can potentially transform the assessment of cardiac function. As it requires successive waves to be combined coherently, this approach is sensitive to high-velocity tissue motion. We investigated coherent compounding of tilted diverging waves, emitted from a 2.5 MHz clinical phased array transducer. To cope with high myocardial velocities, a triangle transmit sequence of diverging waves is proposed, combined with tissue Doppler imaging to perform motion compensation (MoCo). The compound sequence with integrated MoCo was adjusted from simulations and was tested *in vitro* and *in vivo*. Realistic myocardial velocities were analyzed in an *in vitro* spinning disk with anechoic cysts. While a 8 dB decrease (no motion versus high motion) was observed without MoCo, the contrast-to-noise ratio of the cysts was preserved with the MoCo approach. With this method, we could provide high-quality *in vivo* B-mode cardiac images with tissue Doppler at 250 frames per second. Although the septum and the anterior mitral leaflet were poorly apparent without MoCo, they became well perceptible and well contrasted with MoCo. The septal and lateral mitral annulus velocities determined by tissue Doppler were concordant with those measured by pulsed-wave Doppler with a clinical scanner ($r^2 = 0.7, y = 0.9x + 0.5, N = 60$). To conclude, high-contrast echocardiographic B-mode and tissue Doppler images can be obtained with diverging beams when motion compensation is integrated in the coherent compounding process.**

***Index Terms*—Diverging beams, high-frame-rate echocardiography, motion compensation, ultrafast ultrasound imaging.**

I. Introduction

With its wide accessibility, rapid applicability and low cost, transthoracic echocardiography is the premiere modality in cardiovascular imaging. It is also the only imaging modality that allows for dynamic representations of the heart in real time. Nowadays, echocardiography is the gold standard to detect congenital diseases [1], diagnose valvular diseases [2], and assess left ventricular function [3], among others. Conventional two-dimensional echocardiography has been using sequential focused transmits to create a cardiac image line by line (single-line acquisition, see *e.g.,* Fig. 1 in [4]). In the single-line acquisition scheme, the frame rate mainly depends on the image line density, which produces a strong trade-off between temporal resolution and lateral spatial sampling. In practice, 30 to 80 frames per second (fps) are obtained with the single-line acquisition technique in B-mode. This frame rate is usually sufficient for standard diagnosis. It is also generally appropriate for strain imaging at rest, which requires frame rates ideally above 50 fps [5]. Recently developed echocardiographic tools aiming at quantifying mechanical tissue properties or highly transient physiological events, however, require higher frame rates [4], [6]. With the recent advent of high-frame-rate ultrasound imaging (also called "ultrafast ultrasound"), it has become possible to track the electromechanical activity of the myocardium, which can potentially be of interest for the diagnosis of arrhythmia [7], [8]. Estimation of mechanical properties of the myocardial fibers is another promising application [9], [10]. These are only a few of the many expected innovations that will become possible with high-frame-rate ultrasound. This may likely initiate breakthrough clinical advancements in diagnostic ultrasound, especially for motion imaging [4], [11].

To improve imaging rate without deteriorating spatial resolution significantly, multi-line acquisition [12] and multi-line transmit approaches have been proposed (see Fig. 1 in [4]). In the multi-line acquisition method, wider beams are generated and several image lines are produced synchronously [12]. As for the multi-line transmit approach, series of several focused beams (optimally four) are transmitted at the same

Manuscript received December 09, 2015; revised January 26, 2016; accepted January 27, 2016. Date of publication February 03, 2016; date of current version June 26, 2016. This work was supported by an operating grant of the Canadian Institutes of Health Research (CIHR, MOP-106465) and by a pilot project grant of the Quebec Bio-Imaging Network (QBIN) . This project was also partially supported by the Collaborative Health Research program of the Natural Sciences and Engineering Research Council of Canada (CHRP 462240-14) and of CIHR (CPG-134748) . Dr. Garcia held a research scholarship award from the Fonds de Recherche en Santé du Québec (FRSQ). *Asterisk indicates corresponding author.*

This paper has supplementary downloadable material available at http://ieeexplore.ieee.org, provided by the authors.

J. Porée is with the Laboratory of Biorheology and Medical Ultrasonics, Research Center, University of Montreal Hospital, Montreal, QC, H2X 0A9 Canada.

D. Posada is with the Research Unit of Biomechanics and Imaging in Cardiology, University of Montreal Hospital, Montreal, QC, H2X 0A9 Canada.

A. Hodzic and F. Tournoux are with the Department of Echocardiography, University of Montreal Hospital, Montreal, QC, H2L 4M1 Canada.

G. Cloutier are with the Laboratory of Biorheology and Medical Ultrasonics, Research Center, University of Montreal Hospital, Montreal, QC, H2X 0A9 Canada, and also with the Department of Radiology, Radio-Oncology and Nuclear Medicine, and Institute of Biomedical Engineering, University of Montreal, Montreal, QC, H3T 1J4 Canada.

*D. Garcia Research Unit of Biomechanics and Imaging in Cardiology, University of Montreal Hospital, Montreal, QC, H2X 0A9 Canada, and also with the Department of Radiology, Radio-Oncology and Nuclear Medicine, and Institute of Biomedical Engineering, University of Montreal, Montreal, QC H3T 1J4 Canada (e-mail: garcia.damien@gmail.com).

Color versions of one or more of the figures in this paper are available online at http://ieeexplore.ieee.org.

Digital Object Identifier 10.1109/TMI.2016.2523346

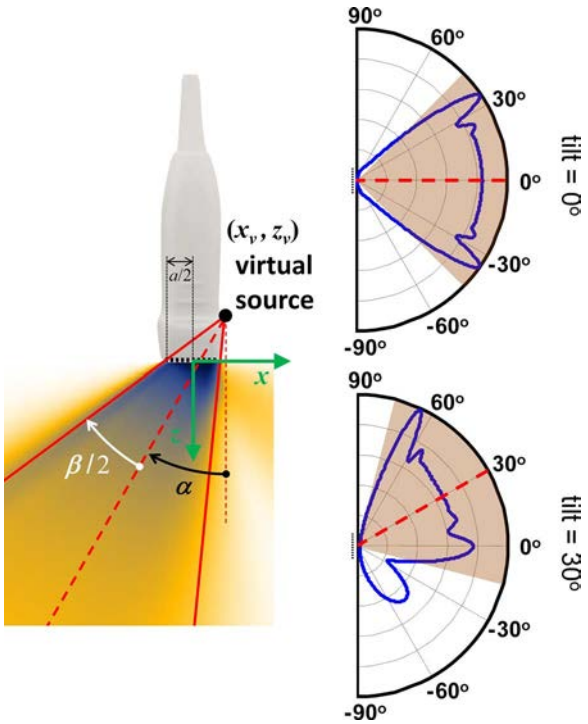

Fig. 1. Description of the diverging circular beams—The circular beams emanated from a virtual source located at (x_v, z_v), in the coordinate system (x, z) associated with the phased-array transducer. The virtual source location was determined by the angular tilt α and width β (see (1)). An angle directed from x to z is of positive sign. The full aperture of the transducer $(= a)$ was used to generate the diverging beams. The polar plots (right column) represent two simulated far-field radiation patterns (normalized root-mean-square acoustic pressure fields) for the 2.5 MHz phased-array used in this study. The sectors of interest were 90°-wide (shaded areas). Note the occurrence of a significant grating lobe at $-50°$ when tilting at 30°.

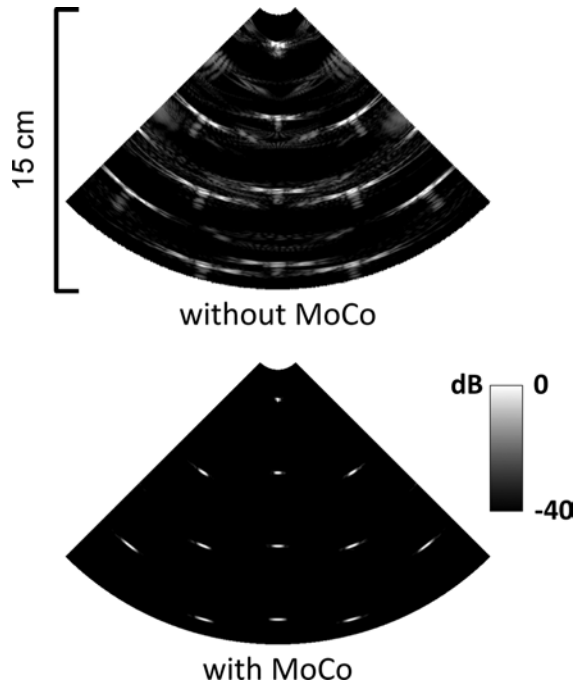

Fig. 2. Compounding with integrated motion compensation—We simulated twelve scatterers moving vertically upward at 15 cm/s. Imaging was performed using 32 wide circular beams, tilted from $-25°$ to 25° (PRF = 4000 Hz). Motion compensation (MoCo) allowed proper focusing (bottom panel).

time [13]. Other advances in beamforming strategies to boost the frame rate for cardiac ultrasound imaging rely on the synthetic aperture focusing technique [14], [15], limited-diffraction-beam-based imaging [16], and plane [17] or diverging wave imaging [18], [19]. Such approaches all imply emissions of unfocused ultrasound wavefronts. In high-frame-rate ultrasound imaging with unfocused transmits, because the acoustic energy is spread onto a broad sector, reconstructed ultrasound images are of poor quality if no additional processing is performed. Several individual bandpass signals, preferably with different obliquities, must therefore be consistently combined ("phase coherent summation" or "coherent compounding") to improve image quality. This can produce an image of comparable quality as conventional focusing [20]. For motionless tissues, phase adjustments determined from the two-way travel times of the ultrasound wave are adequate to reconstruct a given frame. However, if the scatterers move significantly between two transmits, phases may be unaligned and image artifacts may ensue during coherent compounding [21]. In fast-moving tissues, phase delays due to motion must then be taken into account during the compounding process to minimize image degradation.

Compound motion-compensated ultrasound imaging has been inspired by SAR (synthetic aperture radar), a form of airborne radar developed decades ago. To form an image, SAR uses a series of diverging waves whose echoes are coherently combined. In SAR, motion compensation is applied to counterbalance the relative motion between the radar and the target [22]. With the advent of high-frame-rate echography, a few approaches were likewise proposed to offset tissue motion in synthetic aperture ultrasound imaging [23]–[25]. Trahey *et al.* proposed a motion correction based on the cross-correlation of the RF signals to rephase the signals issued from two different receive apertures [23]. Kim *et al.* compared the fast-time cross-correlation with the slow-time Doppler autocorrelation [24]; autocorrelation returned similar results with a much lower computational load. More recently, Gammelmark *et al.* proposed a 2-D motion compensation method by cross-correlating oriented beamformed RF signals to compensate for transducer motion in abdominal applications [25]. In a recent paper, Dénarié *et al.* [26] demonstrated, in a rat heart, the benefits of motion compensation for coherent compound plane wave imaging. To prevent untrue synthetic foci (see Fig. 2 in [26]) generated by a linear transmission sequence (*i.e.,* with linearly increasing tilt angles), Dénarié *et al.* proposed a transmit sequence with tilt angles alternatively negative and positive.

In the present study, we introduce a motion compensation (MoCo) strategy for high-frame-rate transthoracic echocardiography in adults, *i.e.,* using a phased array transducer. Coherent compounding with integrated MoCo is of particular importance in high-frame-rate cardiac imaging since myocardial tissue velocities can be as high as 20 cm/s in normal subjects and athletes [27] (tissue velocities are reduced in cardiopathic subjects). Wide diverging beams were generated using the full aperture of a 2.5 MHz phased-array. To create high-quality B-mode images, a number M of steered circular wavefronts were transmitted using a "triangle sequence". The M corresponding re-

ceived echoes were used both for radial motion estimation and B-mode imaging: the complex envelopes (*i.e.,* $\mathrm{I} + \sqrt{(-1)}\,\mathrm{Q}$, with IQ the in-phase/quadrature signals) were summed coherently by considering the phase delays due to motion. Motion was estimated using a slow-time autocorrelator modified to reduce the adverse effects of sidelobes. The MoCo scheme for high-frame-rate cardiac ultrasound imaging was validated *in vitro* using a rotating disk with speed as high as 30 cm/s. Standard echocardiographic views were also acquired in healthy adult volunteers. High-quality *in vivo* B-mode cardiac images with tissue Doppler were obtained at high temporal resolution (250 frames per second, see the video in the supplementary materials).

II. Theoretical Background

In this section, we describe the transmit sequences (Section II-A) leading to wide diverging beams and introduce our method for motion compensation (Section II-B).

A. Transmit Sequences

1) Delay Laws for Circular Diverging Beams: A number of recent works have reported the feasibility of using large ultrasound wavefronts for *in vivo* cardiac imaging with a transthoracic phased array [18], [19]. In our study, we used a series of circular diverging beams generated by the full array aperture. Our approach was inspired by that of Hasegawa and Kanai [18]. The circular diverging beams were defined by the angular tilt (α) and width (β), both illustrated in Fig. 1. For coherent compounding, only the tilt angle α was modified while the angular width β was kept unchanged. The angular width β was chosen equal to the angular width of the sector of interest. Let a stand for the full effective aperture of the phased-array; basic trigonometry can yield the coordinates (x_v, z_v) of the virtual source leading to an α-tilted β-wide beam in the conventional coordinate system (x, z) associated to the transducer (Fig. 1):

$$\tan\left(\alpha \pm \frac{\beta}{2}\right) = \frac{\pm\frac{a}{2} + x_v}{-z_v}. \tag{1}$$

The transmit delays that must be imposed to the n^{th} array element $(x_n, 0)$ to create a circular beam whose virtual source is located at (x_v, z_v) are written as

$$\Delta\tau_n = \left(\sqrt{(x_n - x_v)^2 + {z_v}^2} - \min_n \sqrt{(x_n - x_v)^2 + {z_v}^2}\right)/c. \tag{2}$$

The parameter c is the speed of sound, assumed to be homogeneous (~ 1540 m/s in soft tissues). The "min" operator ensures that the smallest transmit delay is zero.

2) Tilt Angles: A number of tilted transmits are required to retrieve compound images of sufficient quality. Large tilt angles, however, can generate significant grating lobes. To establish an acceptable steering range when transmitting circular diverging beams with a linear phased-array, we simulated the 2-D root-mean-square (RMS) acoustic pressure in the far-field. These simulations were performed in the frequency domain using Eq. 4.14, p 77 in [28]. Details of the numerical method are given in the supplementary document. We modeled a Philips/ATL P4–2 phased array probe (64 elements, central frequency $= 2.5$ MHz, fractional bandwidth at 6 dB $= 60\%$, pitch $= 0.3$ mm, kerf $= 50$ μm). To give two examples, non-tilted and 30°-tilted 90°-wide RMS pressure far-fields, generated by this simulation, are illustrated in Fig. 1. Such simulations allowed us to determine the maximal tilt angle. The maximal "acceptable" tilt for the P4–2 probe was estimated at 27° (Fig. S1, supplementary document). The tilt angles α_m were thus linearly spaced between $-25°$ and $+25°$. These uniformly spaced tilt angles were ordered in a specific manner ("triangle sequence") to optimize motion estimation and motion compensation, as now clarified.

B. Coherent Compounding and Motion Compensation

1) Adverse Effects of Motion: Since no transmit focusing was performed, coherent compounding of several individual complex envelopes (*i.e.,* IQ signals) was necessary to produce high-contrast ultrasound images. The 90°-wide sector being commonly used in ultrasound cardiac imaging, we focused on this configuration only. Based on the results of numerical simulations in the far-field (see supplementary document, section B, for details), we selected $M = 32$ number of transmits for the *in vitro* and *in vivo* experiments. With such a compounding number, we should expect grating lobe levels smaller than -10 dB (Fig. S2, supplementary document).

Synthetic focusing, as noticeably underlined in [21] and recently in [26], can be significantly affected by the motion of scatterers between transmits, which disturbs coherent compounding and in turn degrades image quality (see Fig. 2, top panel). This can be particularly true in the myocardium where velocities up to 20 cm/s can be observed. Fig. 2 illustrates how tissue motion may deteriorate images: we simulated scatterers moving vertically upward at 15 cm/s using Field II [29], [30]. Imaging was performed using thirty-two 90°-wide circular beams, tilted from $-25°$ to 25°, as described above. Without motion compensation (MoCo), the scatterers are not clearly visible and many artifacts are present (Fig. 2, top). On the other side, the MoCo approach, which is described in the next paragraphs, allowed proper focusing (Fig. 2, bottom). This example points up that it is essential to correct motion-based phase delays to get high-quality B-mode images in high-frame-rate ultrasound echocardiography. Our original MoCo scheme is now introduced.

2) Motion Estimation: For MoCo, we considered a computationally inexpensive approach with the future goal of getting real-time processing and visualization [31]. To determine the phase delays due to radial motion, we used a one-lag slow-time autocorrelation along the M received IQ signals. In some way we used tissue Doppler imaging to estimate motion between successive transmits. To preserve a high Nyquist limit, we did not perform coherent compounding before Doppler estimation (as in [32], [33]; $M(=32)$ successive transmits provided one tissue Doppler image and one motion-compensated B-mode image. Only radial motions were considered since angular resolution in echocardiography is poor relative to radial resolution (due to the small aperture and large depth), especially as depth increases. We slightly modified the autocorrelator to minimize the adverse effects of the sidelobes (called "edge waves" in [26]), as now explained.

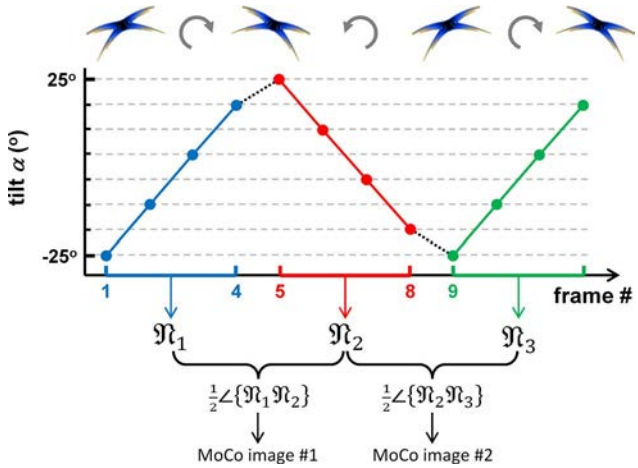

Fig. 3. Triangle transmit sequences & motion estimation—To reduce the side effects due to sidelobes, we used a triangle sequence composed of 32 successive transmits. This figure shows an 8-transmit sequence for clarity. Slow-time autocorrelations were calculated in the ascending and descending stages, and their product was used to estimate the phase delays due to motion. The insets on the top represent the PSFs (point spread functions) with the apparent sidelobes. They rotate in clockwise then counter-clockwise directions.

To generate a single image by coherent compounding with integrated MoCo, $M = 32$ complex envelopes were synthetically focused independently on a fixed 90°-wide polar grid whose pole was the virtual source at tilt $\alpha = 0$. The grid contained 256×256 radial and angular lines, with constant radial and angular steps (*i.e.,* $\Delta\theta = 0.35°$ and $\Delta r \approx$ one wavelength). Assuming that motion was time-invariant during these transmissions, pixelwise motion-induced phase delays were estimated by autocorrelating the slow-time IQ signals. Under this configuration (polar grid + slow-time autocorrelation), only phase delays due to radial motion were considered for MoCo, as mentioned earlier.

For a given ensemble length M, the tilt angles used to produce one compound image were evenly spaced. The way these tilted transmissions must be arranged has some importance. A linear tilt sequence makes the sidelobes move at a nearly constant speed; coherent compounding with integrated MoCo rephases these sidelobes and may thus result in significant image degradation. To reduce these adverse effects, Dénarié *et al.* proposed an alternate transmit sequence with tilt angles alternatively negative and positive [26]. Dénarié's alternate sequence, however, can produce significant artifacts in phase delay estimates due to the repeated reversal of transmission direction. This may cause suboptimal motion-compensated compounding. To eliminate the artifacts due to the sidelobes, we opted for a triangle sequence (see Fig. 3). Two lag-one autocorrelations along the slow-time axis were calculated, both corresponding to the *ascending* and *descending* phases of the triangle sequence, respectively. For M (with M even) tilt angles, the discrete autocorrelations were given by

$$\mathfrak{N}_1(\theta,r) = \sum_{m=1}^{M/2-1} \frac{\widetilde{s_m}\,\overline{\widetilde{s_{m+1}}}}{|\widetilde{s_m}\,\overline{\widetilde{s_{m+1}}}|} \text{ and}$$

$$\mathfrak{N}_2(\theta,r) = \sum_{m=M/2}^{M-1} \frac{\widetilde{s_m}\,\overline{\widetilde{s_{m+1}}}}{|\widetilde{s_m}\,\overline{\widetilde{s_{m+1}}}|}, \quad (3)$$

where, $\widetilde{s_m}(\theta,r)$ stands for the m^{th} slow-time IQ sample (in a total packet of M samples) determined at (θ,r). The transmit-to-transmit phase delays due to motion were estimated using the phase angle of the $\mathfrak{N}_1\mathfrak{N}_2$ product:

$$\phi_{\text{MoCo}}(\theta,r) = \frac{1}{2}\angle\{\mathfrak{N}_1\mathfrak{N}_2\}. \quad (4)$$

The $1/2$ factor in (4) is necessary to recover the phase due to the product of the two autocorrelators; ϕ_{MoCo} is thus in $]-\pi/2,\pi/2]$. As a consequence, the maximum detectable velocity is reduced to $c\,PRF/(8\,f_0)$ (with $PRF =$ pulse repetition frequency, $f_0 =$ carrier frequency), which is half the classical Nyquist Doppler velocity. For a PRF of 4000-5000 Hz and a 2.5 MHz carrier frequency, this corresponds to a Nyquist velocity of 30-38 cm/s, which is about twice the highest myocardial velocities [27]. As shown in the following paragraph, the triangle sequence in adjunction with the autocorrelation product can help to remove most of the adverse effects due to the sidelobes.

3) The Triangle Sequence: Justification: The Doppler autocorrelator (3) uses successive image pairs to estimate velocities. In a compounding series, the successive transmit/receive wavevectors must be preferentially almost equal to minimize signal decorrelation and thus Doppler variance [34]. The linear tilt arrangement $(1,2,\ldots,M)$ is thus an acceptable approach. However, with tilt angles linearly increasing, the sidelobes produced by a single scatterer rotate in the clockwise direction. A cross- or auto-correlation algorithm tracks these sidelobes, which are then rephased if a MoCo scheme is used. This is illustrated in Fig. 4(a). This figure was obtained by simulating a stationary or vertically moving scatterer with Field II. Even in the absence of tissue motion, MoCo induces coherent summation of the sidelobes that become well visible in the real envelopes (Fig. 4(a), 2nd column). Dénarié *et al.* proposed to arrange the tilt angles in an alternate negative-then-positive organization $(1,M,2,M-1,\ldots)$ to sum the sidelobes incoherently [26]. This alternate arrangement, however, reduces the correlation between ultrasound signals and thus increases the variance of the phase-delay estimator (Fig. 4(b), 3rd column). This may induce significant artifacts in motion-compensated real-envelope images (Fig. 4(b), 2rd column). To reduce this undesired effect, Dénarié *et al.* rejected false velocities by thresholding [26].

To remove coherent summation of the sidelobes while getting accurate Doppler velocities, we rather chose two successive linear arrangements which form a triangle sequence $(1,3,5,\ldots,M,M-2,\ldots)$ and which both cover the whole scan area. With the triangle sequence (Fig. 3), the ascending/descending slopes induce clockwise/counter-clockwise rotations of the sidelobes. The autocorrelation product (4) obliterates the phase delays due to these rotations but preserves those issued from tissue motion (see Fig. 4(c), 3rd column). MoCo thus results to a non-coherent summation of the sidelobes (Fig. 4(b), 2nd column). This approach better preserves the original point spread function (no motion, no MoCo) than the linear and alternate sequences.

4) Motion Compensation and Coherent Compounding: We have just seen how phase delays due to radial motion were estimated from the M migrated complex envelopes $\widetilde{s_m}(\theta,r)$. Ad-

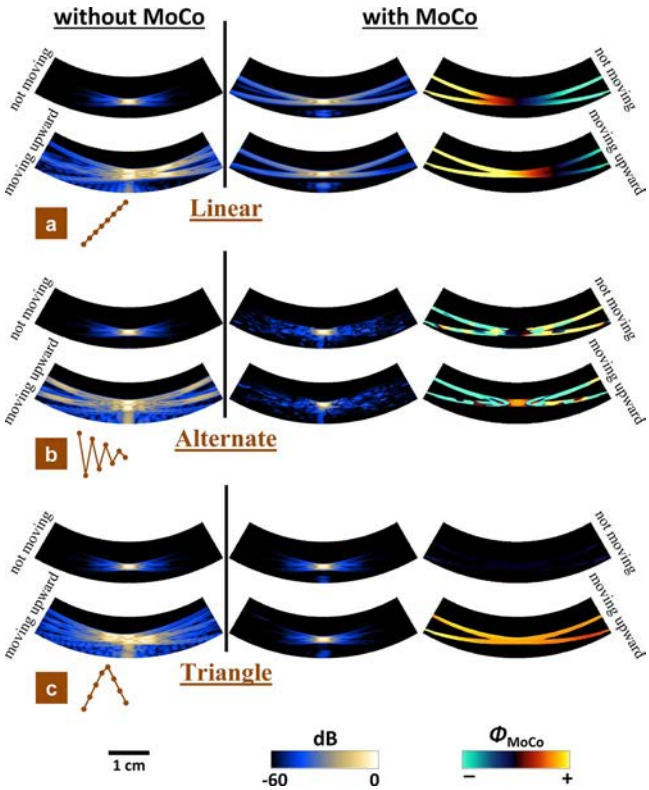

Fig. 4. Linear, alternate and triangle transmit sequences: effect on MoCo—Vertically moving (at 15 cm/s) or non-moving single scatterers were simulated with linear (4.a), alternate (4.b) and triangle (4.c) tilt sequences. The 1st and 2nd columns show the real envelope images without or with MoCo (motion compensation). The 3rd column represents the motion-induced phase delays. Compared to the linear and alternate sequences, the triangle sequence coupled to the autocorrelation product (4) preserves the original point spread function (no motion, no MoCo).

justing then for frame-to-frame displacements and phase rotations yields the coherently compound complex envelop:

$$\tilde{s}_C(\theta, r) = \sum_{m=1}^{M} \left\{ \widetilde{s_m}\left(\theta, r + \left(m - \frac{M}{2}\right) \frac{\phi_{\mathrm{MoCo}}}{4\pi} \frac{c}{f_0}\right) e^{i\, m\phi_{\mathrm{MoCo}}} \right\}. \quad (5)$$

Tissue Doppler velocity is given by the classical Doppler equation:

$$V_{\mathrm{D}} = \frac{PRF\ c}{4\pi\ f_0} \phi_{\mathrm{MoCo}}. \quad (6)$$

The log-compressed modulus of this compound signal gives a motion-compensated B-mode image. Fig. 5 outlines the process for coherent compounding with integrated MoCo.

III. In Vitro and In Vivo Methods

All ultrasound measurements were performed with a Verasonics research scanner (V-1-128, Verasonics Inc., Redmond, WA) and a 2.5 MHz phased-array transducer (ATL P4–2, 64 elements). The raw complex envelopes (IQ data) were sampled at 5 MHz. No apodization was introduced in transmission or reception. The IQ signals were migrated (synthetically focused) using a delay-and-sum and the full receive aperture. A number of 256 radial scanlines (*i.e.*, $\Delta\theta = 0.35°$) were reconstructed

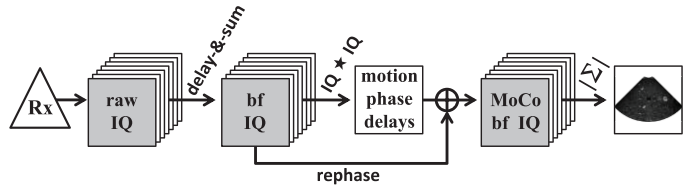

Fig. 5. Coherent compounding with integrated MoCo—Rx = receive, bf = beamformed, MoCo = motion compensation. The five-point star represents the autocorrelation. 1) A series of M tilted beams arranged in a triangle sequence is transmitted. 2) M raw complex envelope (IQ, in-phase and quadrature) images are obtained. 3) These M complex envelopes are migrated to get beamformed complex images (bf IQ). 4) Slow-time autocorrelations return the phase delays due to tissue motion. 5) These phase delays are used to rephase the beamformed complex images and get motion-compensated beamformed complex images (MoCo bf IQ). 6) The motion-compensated beamformed complex images are summed; the modulus of the resulting image is log-compressed to give a B-mode image.

during migration, at a radial sampling of 1 wavelength, both *in vitro* and *in vivo*.

A. In Vitro Experiments Without Motion

In vitro experiments were first performed without motion to confirm the number of compounding tilt angles required for getting 90°-wide B-mode images of good quality. We expected the experimental results to be concordant with the numerical predictions described in the supplementary document. We used a tissue mimicking phantom (Gammex, model 403GS LE). A number of M tilted 90°-wide circular wavefronts were emitted using the transmit delays given by (1) and (2). Short bursts of 2 wavelengths were transmitted at a pulse repetition frequency (PRF) of 4000 Hz. Tilt angles were linearly spaced from $-25°$ to 25°, with a total number of $M = 2, 4 \ldots 48$. Because no motion was considered in these experiments, the tilt arrangement was of no importance. After migration, the M IQ signals were coherently summed and the resulting real envelope signals were log-compressed. We estimated the contrast-to-noise-ratio (CNR) [35] of the 1-cm-diameter 6-cm-deep anechoic cyst:

$$\mathrm{CNR} = 20 \log_{10} \frac{|\mu_{\mathrm{cyst}} - \mu_{\mathrm{bg}}|}{\sqrt{(\sigma^2_{\mathrm{cyst}} + \sigma^2_{\mathrm{bg}})/2}}, \quad (7)$$

where μ_{cyst} and μ_{bg} (σ^2_{cyst} and σ^2_{bg}) are the means (variances) of the grayscale intensities in the cyst and the background regions, respectively. For comparison, a reference B-mode image was also generated using a series of 128 steered scanlines focused at 6 cm.

B. In Vitro Experiments With Motion

We tested our MoCo approach on a 10-cm-diameter tissue-mimicking spinning disk. This disk was mounted on a step motor assembly allowing control of its rotational speed. The weight composition of the tissue-mimicking disk was agar 3%, Sigmacell cellulose powder 3%, glycerol 8% and water. Four equidistant 1.5-cm-diameter anechoic cysts were located at 3.5 cm from the disk center. The phantom rotated at angular velocities ranging from 0 to 6 radians per second (with an increment of 0.5), which gave a maximum outer speed of ~30 cm/s. For each rotation speed, the disk was insonified with series of $M = 32$ tilted 90°-wide circular wavefronts. The

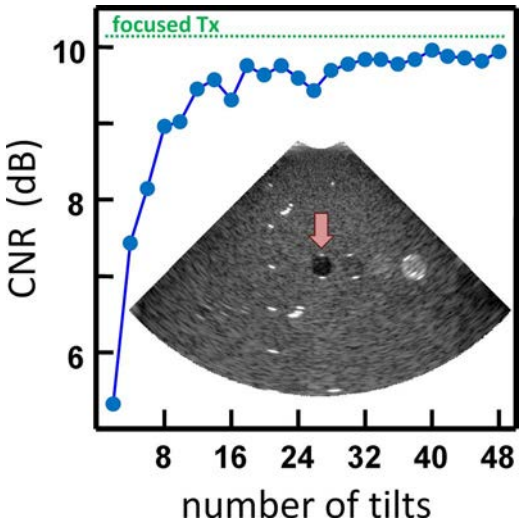

Fig. 6. Cyst contrast as a function of total number of tilts—Gammex experiments were first performed without motion. The tilt angles were linearly spaced between $-25°$ and $25°$. No significant improvement of CNR (contrast-to-noise ratio) was observed above 32 tilt angles. The thick arrow points out the analyzed anechoic cyst. The dashed line gives the reference CNR returned by the focused transmits.

packet length $M = 32$ was chosen after analysis of the results issued from the simulations (see supplementary document) and Gammex-derived *in vitro* experiments (Fig. 6). Tilt angles were ordered according to the abovementioned triangle sequence (Fig. 3). After migration, pixelwise slow-time lag-one autocorrelations were determined in both the ascending and descending phases of the triangle sequence ($\mathfrak{N}_1$ and $\mathfrak{N}_2$, ensemble lengths $= M/2 = 16$; see Fig. 3) and the product $\mathfrak{N}_1\mathfrak{N}_2$ was smoothed using a 5×3 Hamming moving spatial average filter ($\sim$ 2 wavelengths in the radial direction, and $0.5°$ in the angular direction). The phase of the smoothed correlation product was then determined (4) for subsequent MoCo. The experiments were repeated with linear and alternate tilt arrangements for comparison.

To verify the effect of angular motion on MoCo, we estimated the CNR (7) of both the south and north-east anechoic cysts in the B-mode images: the south cyst has a null radial velocity and a maximal angular velocity, while the north-east cyst has a null angular velocity and a maximal radial velocity. CNR with or without MoCo were compared. The root-mean-square error of the estimated Doppler velocity, normalized to the maximal speed (NRMSE), was also calculated using the ground-truth Doppler velocities of the rotating phantom. We finally analyzed the effect of noise on Doppler estimates: different levels of white Gaussian noise were added to the raw IQ data issued from the disk rotating at 4 rad/s.

C. Motion-Compensated Echocardiography

In vivo cardiac cineloops were obtained in a 30 y-o healthy volunteer. Two classical views were examined: apical long-axis 4-chamber and parasternal long-axis views. The transmit sequences were similar to those used *in vitro* (with the triangle transmission sequence). Coherently-compounded B-mode images were generated with or without MoCo and compared, as explained above. Since we used a 32-sample sliding window with 50% overlap (Fig. 3), an efficient frame rate of 250 images/s was obtained (PRF/16 = 4000/16 = 250). A 2^{nd} order polynomial regression filter was used to reduce clutter components. Quality of the B-mode images obtained with or without MoCo was compared visually. Apical long-axis 4-chamber views were also acquired with the linear, alternate and triangle sequences for comparison. When switching from one tilt sequence to the other, the probe was maintained in the same position. The septal and lateral mitral annulus velocities given by the modified autocorrelator with the Verasonics scanner ((3) + (4)) were also compared with those of a GE Vivid q scanner (pulsed-wave tissue Doppler imaging) in the apical 4-chamber view of 10 healthy volunteers. Tissue Doppler velocities were determined at peak systole, left ventricular relaxation and atrial contraction (S'-, e'- and a'-waves). A total of 60 measures per technique (GE *vs*. Verasonics scanner) were available (2 walls $\times$ 3 peak velocities $\times$ 10 subjects). The conventional and MoCo-based tissue velocities were measured by two blinded operators. Correlation and agreement were analyzed by linear regression and Bland-Altman plot. The protocol was approved by the human ethical review committee of the CRCHUM.

IV. Results

A. In Vitro Experiments Without Motion

The contrast-to-noise ratio (CNR) of the Gammex's anechoic cysts improved significantly ($\sim$ 4-dB increase) when increasing the number of tilt angles (Fig. 6). In accordance with the numerical simulations (Fig. S2, supplementary document), this improvement, however, became less significant above a total number of $\sim$32 tilt angles (CNR $>$ 9.5 dB). The CNR then was close to that returned by the focused transmits ($\sim$10 dB).

B. In Vitro Experiments With Motion

The images of the spinning disk show that the contrast of the cysts degraded rapidly, as speed increased, if no MoCo was performed (Figs. 7 and 8). This was particularly true for the north-east cyst (from 7 dB down to 0 dB, Fig. 8, left panel) whose radially projected velocities were maximal. When triangle sequences and MoCo were integrated to coherent compounding, high-quality images were obtained (Fig. 7) and MoCo was able to recover the $\sim$ 7 dB contrast level, regardless of the rotation speed (Fig. 8). This was true for both the south (right panel) and north-east (left panel) cysts. Since the south cyst had null radial velocity and maximal angular velocity, this confirms that mostly radial correction was necessary during MoCo in our echocardiographic context.

Although cyst CNR was almost equivalent for the three tilt sequences (linear, alternate & triangle), more artifacts were present in the B-mode and Doppler images with the linear and alternate sequences (see Fig. S3 in the supplementary content). With the linear sequence, artifacts were visible in the background since MoCo tends to rephase the sidelobes (see Fig. 4(a)); with numerical simulations of the alternate sequence (see Fig. 4(b)), destructive interferences were present in the disk due to imprecise velocity measures. The triangle transmission sequence proposed here returned the most accurate and precise Doppler velocities (Fig. 9). The effect of

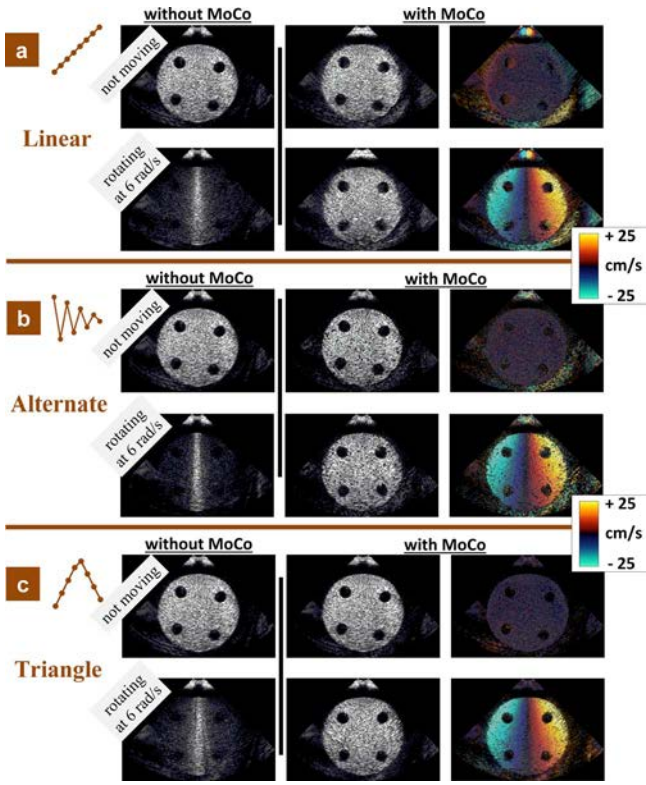

Fig. 7. In vitro experiments (disk)—In vitro experiments were performed with motion, in a disk rotating at angular velocities ranging from 0 to 6 rad/s (maximum outer speed of $\sim$ 30 cm/s). Linear (7.a), alternate (7.b) and triangle (7.c) tilt sequences were tested. The 1st and 2nd columns show the real envelope images without or with MoCo (motion compensation), respectively. The 3rd column represents the estimated tissue Doppler velocities.

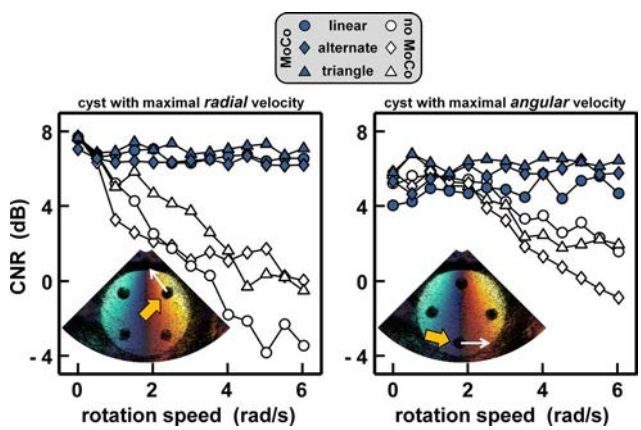

Fig. 8. Effect of speed on cyst contrast. (In vitro experiments in a spinning disk, see Fig. 7)—Linear (circles), alternate (diamonds) and triangle (triangles) transmit sequences were tested. The thick arrows point out the analyzed anechoic cyst at maximum radial velocity (left) and maximum azimuthal velocity (right). The thin white arrows represent the local velocity vectors.

noise on Doppler estimation became insignificant beyond a SNR of 15–20 dB (Fig. 9, top-right panel). Consequently, since MoCo depends directly on the Doppler estimates, the quality of the motion-compensated B-mode images was robust to noise (Fig. 9, 2nd row). Overall, the results revealed that our MoCo-based approach enables high-contrast imaging of fast-moving objects using circular diverging beams.

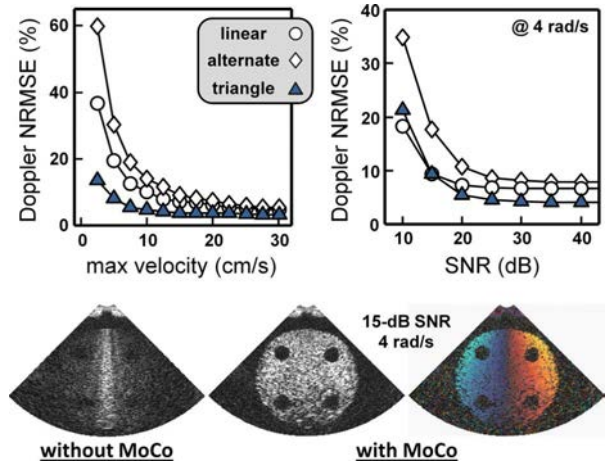

Fig. 9. Effect of speed and noise on Doppler estimates—Doppler NRMSE *vs.* speed (top-left panel): same data as in Fig. 8. Doppler NRMSE *vs.* noise (top-right panel): white Gaussian noise was added to the raw IQ *in vitro* data before beamforming and compounding (data at 4 rad/s). The 2nd row illustrates the effect of MoCo on low-SNR data (15 dB).

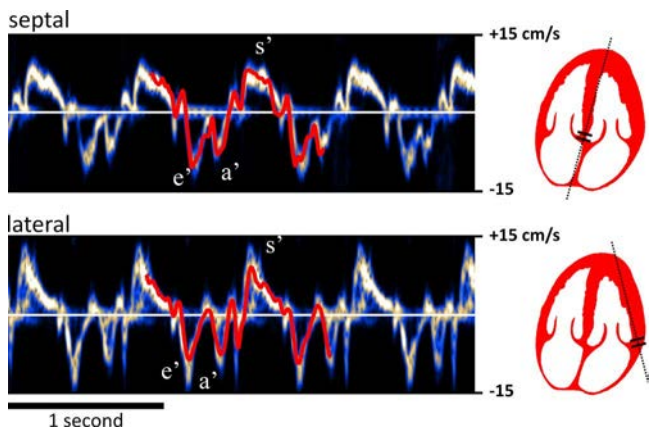

Fig. 10. Mitral annulus velocities—The septal and lateral mitral annulus velocities of a healthy volunteer were measured by PW-TDI (pulsed-wave tissue Doppler imaging) with a GE clinical scanner. The thick solid red curves represent the mitral annulus velocities determined by our modified autocorrelator in the same volunteer ((6), see also Fig. 13 top-right). S'-wave: peak systole; e'-wave: left ventricular relaxation; a'-wave: left atrial contraction.

C. *Motion-Compensated Echocardiography*

The septal and lateral mitral annulus velocity waveforms returned by the modified autocorrelator were comparable to those returned by the GE-scanner pulse-wave Doppler mode (Figs. 10 and 11). A high correlation ($r^2 = 0.70$, Fig. 11 left) and a good agreement were observed between the two techniques and no proportional bias was detected (average bias $= -0.54$ cm/s, Fig. 11 right). MoCo also improved the quality of the *in vivo* cardiac images returned by transthoracic high-frame-rate echocardiography (Fig. 12). This was particularly visible in the apical 4-chamber view during peak systole, left ventricular relaxation and atrial contraction (Fig. 10). For example, at peak S'-wave, although the septum and the anterior mitral leaflet were poorly apparent without MoCo (Fig. 12, top-left), they became well perceptible and well contrasted with MoCo (Fig. 12, top-middle). MoCo outcome was also well perceptible in the parasternal long-axis view (Fig. 12, second row). When inspecting the tissue Doppler velocities measured during the MoCo process (Fig. 12,

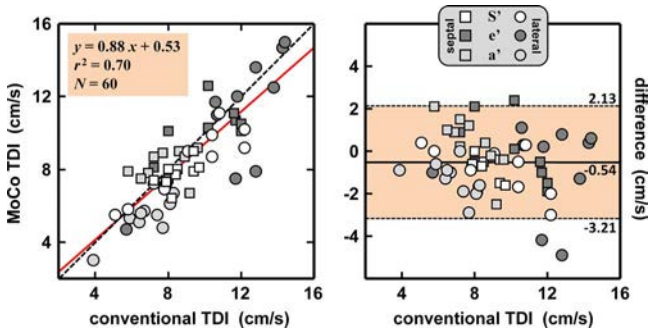

Fig. 11. Mitral annulus velocities: comparison with conventional TDI—The septal and lateral mitral annulus peak velocities of 10 healthy volunteers were measured by conventional PW-TDI (pulsed-wave tissue Doppler imaging) with a GE clinical scanner. They were also determined by our modified autocorrelator using circular wave transmissions (MoCo TDI). See Fig. 10 for one example. Left panel: The solid line is the regression line. Right panel: the shaded area represents the ± 2 standard-deviations interval.

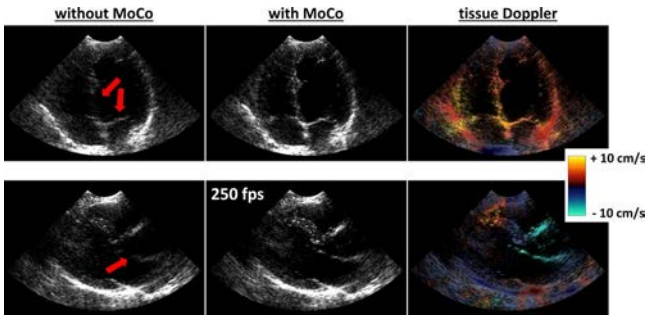

Fig. 12. Motion-compensation for high-contrast high-frame-rate echocardiography of the left ventricle—The sequence described in this study (32 90°-wide circular diverging beams, tilts from $-25°$ to $+25°$, triangle sequence, 250 frames/s) was tested in the left ventricle of a healthy volunteer. Coherent compounding was performed without or with MoCo. The thick arrows indicate regions where MoCo had critical advantages. The 3rd column displays tissue Doppler images measured during the MoCo process (Eq. 8). In general, the effect of MoCo was more manifest in fast-moving tissues. Top row: apical 4-chamber view at peak systole; bottom row: parasternal long-axis view at peak systole. Online movies are also available in the supplementary materials.

rightmost column), it is noticeable that MoCo had significant effects in fast-moving regions. Online movies are available in the supplementary materials for a comparison without/with MoCo during a whole cardiac cycle. Because Doppler artifacts were present, the linear and alternate sequences resulted in artefactual B-mode images (Fig. 13) in comparison with the triangle sequence: sidelobes were present in the lateral endocardium with the linear sequence and incoherent interferences were visible with the alternate sequence.

V. Discussion

In this study, we used tilted circular diverging beams to produce wide-sector high-contrast echocardiographic images at 250 frames per second. We obtained a five-fold increase in frame rate compared with conventional clinical scanners. As revealed by *in vitro* and *in vivo* data, motion compensation (MoCo) was a *sine qua non* when imaging fast-moving tissues from coherently compounded signals. To compensate for motion, we proposed a triangle transmit sequence with a modified slow-time autocorrelator. This option allowed us to minimize the artifacts due to the sidelobes. With MoCo, the

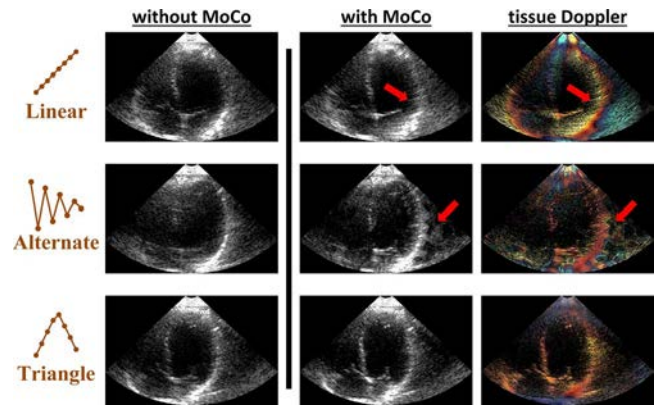

Fig. 13. Motion-compensation for echocardiography of the left ventricle: effect of tilt sequence—The acquisition protocol was the same as in the previous figure (apical 4-chamber view, here at peak systole), except that linear and alternate sequences were also tested. The linear and triangle sequences induced artifacts in both B-mode images (2nd column) and tissue Doppler (rightmost column). The thick arrows indicate artifacts generated by the linear and alternate sequences.

in vitro spinning-disk results showed that CNR ratios could be preserved even at the highest velocities (30 cm/s). These findings were confirmed by *in vivo* echocardiograms of the left ventricle. Without MoCo, high-contrast images could not be obtained during rapid contraction: the basal ventricular septum and mitral leaflets were poorly contrasted or barely visible.

A. Getting Accurate and Precise Motion Estimation

In this study, we had to face a dilemma: on the one hand, uncorrelated signals are preferred to get high-contrast B-mode images, but on the other hand, partially correlated signals must be favored to reduce the variance of the phase delay estimates, as established by the Cramér-Rao bound [34]. A compromise can be found if the wavevectors of two successive transmissions are sufficiently close. To this purpose, the transmission tilt sequence that might come to mind is the linear arrangement tested in this study and in [26]. Linear sequences, however, induce a regular motion of the sidelobes due to the regularly spaced tilts. After MoCo, these sidelobes are coherently summed and could become visible. The simulations in Fig. 4 clearly illustrate this unwanted effect, which can have negative impacts *in vivo*. For example, in the case reported in Fig. 13 (1st row), the sidelobe velocities corrupted tissue Doppler; as a result, the sidelobes became apparent due to their coherent summation, especially near the myocardium. The alternate tilt sequence proposed by Dénarié *et al.* prevents coherent summation of the sidelobes, as can be noticed in Fig. 4(b). Such a positive/negative arrangement, however, strongly decorrelates the successive received signals, thus resulting in high Doppler variances. Due to the presence of spurious motion estimates, this could affect MoCo and deteriorate B-mode imaging (Fig. 13, 2nd row). To optimize the alternate MoCo approach in the context of plane wave imaging, Dénarié *et al.* rejected unrealistically high velocities as well as velocities with high variances [26]. To sum up, linear sequences lead to inaccurate motion estimates (biases due to sidelobe motion), while alternate sequences generate imprecise motion estimates (large variance due to poorly correlated signals). To get high-quality compound images, sidelobes must be

summed incoherently. To obtain an efficient MoCo, sidelobe velocities should therefore be equal to the mainlobe velocities. To this purpose and to increase both accuracy and precision in motion estimation, we proposed a triangle sequence (Fig. 3) where tilts increase then decrease linearly. Such a sequence is composed of two linear sequences, each with relatively good precision but low accuracy. To gain accuracy, we thus introduced the autocorrelation product (4) to remove the bias due to sidelobe motion. As shown by the *in vivo* results (Figs. 11 and 12), the triangle sequence with the autocorrelation product seems to be well adapted for echocardiography. Of note, this approach is not limited to diverging waves only and could be adapted for plane wave imaging.

B. 1-D Versus 2-D MoCo

Like Dénarié *et al.* who studied MoCo for plane wave imaging [26], we only compensated radial motions. To estimate the phase delays due to motion, we used a numerical approach similar to tissue Doppler's, the major difference being the autocorrelation product coupled to a triangle transmit sequence. MoCo using full 2-D motion components has been proposed by Gammelmark *et al.* in subaperture-based STA (synthetic transmit aperture) imaging [25]. Gammelmark's MoCo scheme implies time-domain cross-correlation of high-resolution lines acquired at multiple angles. This approach provides a low frame rate and the associated motion estimator is much more computationally expensive than the Doppler-based scheme used in our study, which could limit real-time implementation [31]. Ekroll *et al.* [33] used the vector Doppler technique proposed by Yiu *et al.* [36] to compensate for 2-D motion. Although well suited to linear arrays, this approach would result in ill-conditioned matrices ((2) in [36]) with phased arrays due to the small size of the receive aperture [37]. Previous studies with uniform linear arrays pointed out that mostly radial motion might be taken into consideration for MoCo [21], [23], [26]. We also chose 1-D MoCo since cross-range resolution was small relative to axial resolution, especially as depth increases. By neglecting the cross-range motion, however, motion blur can be introduced in the angular direction for large frame-to-frame displacements. For example, at $r = 7.5$ cm, the cross-range resolution at best is $\lambda r/a = 2.4$ mm. For an angular tissue velocity of 15 cm/s and a PRF of 4000 Hz, the total displacement during 32 successive transmits is 1.2 mm, which is half the cross-range resolution. In our *in vitro* experiments, excluding cross-range motion in MoCo had little effect on the quality of compound sector images. This was noticeable in the spinning disk experiments, where contrast was no longer motion-dependent after radial MoCo (Fig. 8). Fig. 8 also shows that the south cyst (with maximal angular velocity and null radial velocity) was well-contrasted after radial MoCo. It was also confirmed by the high-quality B-mode echocardiographic images (Figs. 12 and 13).

C. Simultaneous B-Mode and Tissue Doppler Imaging

High-contrast imaging of the heart based on unfocused transmits was practically unfeasible without MoCo in our *in vivo* acquisitions during rapid cardiac filling/contraction. Our findings and others' [14], [25], [26] indeed show that MoCo is required to obtain high-contrast ultrasound images if coherent compounding is brought into play. Fast cardiac imaging was also recently evaluated using an alternative mode based on multi-transmit beamforming [38]. In this technique, simultaneous focused or narrow beams (2 to 6 in practice) are transmitted into different directions leading to a severalfold increase in frame rate [13]. Combined with multi-line acquisition, frame lag can be further decreased [38]. Since beams are focused, an advantage of multi-line transmit imaging is that it does not entail coherent compounding and MoCo. However, the main and side lobes of the different beams might interfere and produce crosstalk artifacts and contrast loss. These artifacts can be significantly reduced with a proper transmit apodization [38] or using the 2^{nd} harmonic signal [39].

Similarly, our technique has the advantage to provide B-mode echocardiography with both high contrast and high frame rates. Another benefit is the inherent tissue Doppler modality that can be produced. We indeed obtained simultaneous B-mode and tissue Doppler imaging of the whole left and right ventricles at high frame rates (250 fps). In comparison, 100 fps is a typical frame rate of tissue Doppler imaging with a clinical scanner for the left ventricle only (*i.e.,* with a narrower sector). The spectral tissue Doppler waveform of the GE Vivid q was sampled at ~ 400 Hz. As a comparison, this corresponds to a sampling frequency that could be obtained with our transmit scheme using $\mathrm{PRF} = 5000$ Hz and $M = 24$. Note however that spectral tissue Doppler can only measure local velocities asynchronously while we obtained a full 2-D map of the myocardium. Clinical applications of tissue Doppler imaging include assessment of left ventricular systolic and diastolic functions. Similar to mitral inflow, the mitral annulus velocity has two waves (called e' and a', Fig. 10) during diastole, which represent early and late diastolic filling, respectively. Diastolic function can be assessed by comparing the mitral inflow and annulus dynamics [40]. In clinical practice, the velocity of the mitral annulus is measured by pulsed wave tissue Doppler in a four chamber view. In 10 healthy volunteers, the septal and lateral mitral annulus velocities estimated by our method were very concordant with those determined with a clinical GE portable scanner (Fig. 11). Although further investigation is needed, this shows that our approach can return accurate tissue Doppler velocities. The main limitation of tissue Doppler imaging is, however, its angle dependence. In addition, tissue Doppler imaging cannot discriminate passive motion (translation and tethering) from active motion (fiber contraction or relaxation). Implementing strain imaging in the current framework may provide a means to evaluate local contractility. High frame rates indeed make frame-to-frame displacements smaller and can thus allow the use of more accurate and more robust strain estimators based on advanced optical flow methods [41], [42]. We have recently used such an approach in vascular strain imaging [42] and a similar method could be adapted to high-frame-rate cardiac imaging.

D. Limitations and Potential Improvements

In ultrasound imaging with unfocused beams, a substantial number of tilted transmits is required for image compounding;

image quality must be improved at the expense of temporal resolution. In our configuration, we found that 32 transmits was a good compromise to generate one 90°-wide image. Using a PRF of 4000 Hz and a 50% slow-time overlap, we have shown that Doppler-based MoCo with a "triangle" sequence can provide high-quality images of the myocardium at 250 fps (see Figs. 12–13). A few limitations, however, must be pointed out.

i) Because the proposed MoCo approach is based on the Doppler autocorrelator, it is prone to aliasing. In the present study, the Nyquist limit was $\sim$ 30 cm/s (see paragraph Section II-B2) which is high enough for imaging the myocardium dynamics. The mitral leaflets, however, can reach higher velocities during the left ventricular early filling. In this case, MoCo may induce destructive interferences and make parts of the valvular leaflets disappear.

ii) Doppler estimators are sensitive to clutter noise. Signals arising from adjacent tissue structures, moving at different velocities and/or in different directions, may introduce a bias in the local velocity estimates and thus corrupt MoCo. In this study, we used a second order polynomial regression filter to reject clutter. Although we got accurate velocity estimates in most situations (Fig. 11), SVD clutter filters could also be used for a better assessment of tissue velocities [43].

iii) The accuracy of tissue Doppler also depends on the system characteristics and noise level [34]. As the acoustic energy of diverging beams spreads with depth, Doppler estimation becomes more sensitive to noise. Tissue Doppler and MoCo might thus become inaccurate. One way to reduce this side effect is to increase the correlation between successive signals using smaller steering angles and/or longer transmitted pulses, but at the expense of lateral and axial resolutions.

iv) The lack of energy focusing in transmit, due to the use of successive tilted diverging beams, also limits the generation of higher harmonics as used in high contrast imaging. Second harmonic generation using diverging beams needs to be investigated to evaluate the feasibility of high-frame rate tissue harmonic imaging.

VI. Conclusion

High-contrast echocardiographic images could be obtained from diverging beams when motion compensation was integrated in the coherent compounding process. High-frame-rate echocardiography could improve cardiac diagnosis from a better analysis of myocardial motion.

References

[1] L. Mertens and M. K. Friedberg, "The gold standard for noninvasive imaging in congenital heart disease: echocardiography," *Curr. Opin. Cardiol.*, vol. 24, no. 2, pp. 119–124, 2009.

[2] P. Pibarot, D. Garcia, and J. G. Dumesnil, "Energy loss index in aortic stenosis: From fluid mechanics concept to clinical application," *Circulation*, vol. 127, no. 10, pp. 1101–1104, 2013.

[3] S. F. Nagueh *et al.*, "Recommendations for the evaluation of left ventricular diastolic function by echocardiography," *Eur. J. Echocardiogr.*, vol. 10, no. 2, pp. 165–193, 2009.

[4] M. Cikes, L. Tong, G. R. Sutherland, and J. D'hooge, "Ultrafast cardiac ultrasound imaging: technical principles, applications, and clinical benefits," *JACC, Cardiovasc. Imag.*, vol. 7, no. 8, pp. 812–823, 2014.

[5] H. Blessberger and T. Binder, "Two dimensional speckle tracking echocardiography: basic principles," *Heart*, vol. 96, no. 9, pp. 716–722, 2010.

[6] M. Tanter and M. Fink, "Ultrafast imaging in biomedical ultrasound," *IEEE Trans. Ultrason., Ferroelectr. Freq. Control*, vol. 61, no. 1, pp. 102–119, Jan. 2014.

[7] H. Kanai, "Propagation of vibration caused by electrical excitation in the normal human heart," *Ultrasound Med. Biol.*, vol. 35, no. 6, pp. 936–948, 2009.

[8] J. Provost *et al.*, "Electromechanical wave imaging for arrhythmias," *Phys. Med. Biol.*, vol. 56, no. 22, pp. L1–11, 2011.

[9] M. Couade *et al.*, "In vivo quantitative mapping of myocardial stiffening and transmural anisotropy during the cardiac cycle," *IEEE Trans. Med. Imag.*, vol. 30, no. 2, pp. 295–305, Feb. 2011.

[10] H. Kanai, "Propagation of spontaneously actuated pulsive vibration in human heart wall and in vivo viscoelasticity estimation," *IEEE Trans. Ultrason., Ferroelectr., Freq. Control*, vol. 52, no. 11, pp. 1931–1942, Nov. 2005.

[11] B. Brekke *et al.*, "Ultra-high frame rate tissue doppler imaging," *Ultrasound Med. Biol.*, vol. 40, no. 1, pp. 222–231, 2014.

[12] D. P. Shattuck, M. D. Weinshenker, S. W. Smith, and O. T. V. Ramm, "Explososcan: a parallel processing technique for high speed ultrasound imaging with linear phased arrays," *J. Acoust. Soc Am.*, vol. 75, no. 4, pp. 1273–1282, 1984.

[13] R. Mallart and M. Fink, "Improved imaging rate through simultaneous transmission of several ultrasound beams," in *Proc. SPIE*, 1992, vol. 1733, pp. 120–130.

[14] L. P. Nock and G. E. Trahey, "Synthetic receive aperture imaging with phase correction for motion and for tissue inhomogeneities. I. Basic principles," *IEEE Trans. Ultrason., Ferroelectr. Freq. Control*, vol. 39, no. 4, pp. 489–495, Jul. 1992.

[15] J. A. Jensen, S. I. Nikolov, K. L. Gammelmark, and M. H. Pedersen, "Synthetic aperture ultrasound imaging," *Ultrasonics*, vol. 44, pp. E5–15, 2006.

[16] J. Lu, J. Cheng, and W. Jing, "High frame rate imaging system for limited diffraction array beam imaging with square-wave aperture weightings," *IEEE Trans. Ultrason., Ferroelectr., Freq. Control*, vol. 53, no. 10, pp. 1796–1812, Oct. 2006.

[17] L. Tong, H. Gao, H. F. Choi, and J. D'hooge, "Comparison of conventional parallel beamforming with plane wave and diverging wave imaging for cardiac applications: a simulation study," *IEEE Trans. Ultrason. Ferroelectr. Freq. Control*, vol. 59, no. 8, pp. 1654–1663, Aug. 2012.

[18] H. Hasegawa and H. Kanai, "High-frame-rate echocardiography using diverging transmit beams and parallel receive beamforming," *J. Med. Ultrason.*, vol. 38, no. 3, pp. 129–140, 2011.

[19] C. Papadacci, M. Pernot, M. Couade, M. Fink, and M. Tanter, "High-contrast ultrafast imaging of the heart," *IEEE Trans. Ultrason., Ferroelectr., Freq. Control*, vol. 61, no. 2, pp. 288–301, Feb. 2014.

[20] G. Montaldo, M. Tanter, J. Bercoff, N. Benech, and M. Fink, "Coherent plane-wave compounding for very high frame rate ultrasonography and transient elastography," *IEEE Trans. Ultrason. Ferroelectr. Freq. Control*, vol. 56, no. 3, pp. 489–506, Mar. 2009.

[21] J. Wang and J. Y. Lu, "Motion artifacts of extended high frame rate imaging," *IEEE Trans. Ultrason., Ferroelectr., Freq. Control*, vol. 54, no. 7, pp. 1303–1315, Jul. 2007.

[22] J. C. Kirk, Jr, "Motion compensation for synthetic aperture radar," *IEEE Trans. Aerosp. Electron. Syst.*, no. 3, pp. 338–348, May 1975.

[23] G. E. Trahey and L. F. Nock, "Synthetic receive aperture imaging with phase correction for motion and for tissue inhomogeneities. II. Effects of and correction for motion," *IEEE Trans. Ultrason., Ferroelectr., Freq. Control*, vol. 39, no. 4, pp. 496–501, Jul. 1992.

[24] K. S. Kim, J. S. Hwang, J. S. Jeong, and T. K. Song, "An efficient motion estimation and compensation method for ultrasound synthetic aperture imaging," *Ultrason. Imag.*, vol. 24, no. 2, pp. 81–99, 2002.

[25] K. Gammelmark and J. Jensen, "2-D tissue motion compensation of synthetic transmit aperture images," *IEEE Trans. Ultrason., Ferroelectr., Freq. Control*, vol. 61, no. 4, pp. 594–610, Apr. 2014.

[26] B. Denarie *et al.*, "Coherent plane wave compounding for very high frame rate ultrasonography of rapidly moving targets," *IEEE Trans. Med. Imag.*, vol. 32, no. 7, pp. 1265–1276, Jul. 2013.

[27] S. F. Nagueh, K. J. Middleton, H. A. Kopelen, W. A. Zoghbi, and M. A. Quiñones, "Doppler tissue imaging: A noninvasive technique for evaluation of left ventricular relaxation and estimation of filling pressures," *J. Am. Coll. Cardiol.*, vol. 30, no. 6, pp. 1527–1533, 1997.

[28] L. W. Schmerr, *Fundamentals of Ultrasonic Phased Arrays*. New York: Springer, 2015.
[29] J. A. Jensen, "Field: A program for simulating ultrasound systems," *Med. Biol. Eng Comput.*, vol. 34, pp. 351–353, 1996.
[30] J. A. Jensen and N. B. Svendsen, "Calculation of pressure fields from arbitrarily shaped, apodized, and excited ultrasound transducers," *IEEE Trans. Ultrason. Ferroelectr. Freq. Control*, vol. 39, no. 2, pp. 262–267, Mar. 1992.
[31] C. Moore *et al.*, "Live high-frame-rate echocardiography," *IEEE Trans. Ultrason., Ferroelectr., Freq. Control*, vol. 62, no. 10, pp. 1779–1787, Oct. 2015.
[32] J. Bercoff *et al.*, "Ultrafast compound doppler imaging: providing full blood flow characterization," *IEEE Trans. Ultrason. Ferroelectr. Freq. Control*, vol. 58, no. 1, pp. 134–147, Jan. 2011.
[33] I. K. Ekroll, M. M. Voormolen, O. K. V. Standal, J. M. Rau, and L. Lovstakken, "Coherent compounding in doppler imaging," *IEEE Trans. Ultrason., Ferroelectr., Freq. Control*, vol. 62, no. 9, pp. 1634–1643, Sep. 2015.
[34] W. F. Walker and G. E. Trahey, "A fundamental limit on delay estimation using partially correlated speckle signals," *IEEE Trans. Ultrason., Ferroelectr., Freq. Control*, vol. 42, no. 2, pp. 301–308, Mar. 1995.
[35] M. C. v. Wijk and J. M. Thijssen, "Performance testing of medical ultrasound equipment: Fundamental vs. harmonic mode," *Ultrasonics*, vol. 40, no. 1-8, pp. 585–591, 2002.
[36] B. Y. Yiu, S. S. Lai, and A. C. Yu, "Vector projectile imaging: time-resolved dynamic visualization of complex flow patterns," *Ultrasound Med. Biol.*, vol. 40, no. 9, pp. 2295–2309, 2014.
[37] M. Tanter, J. Bercoff, L. Sandrin, and M. Fink, "Ultrafast compound imaging for 2-D motion vector estimation: application to transient elastography," *IEEE Trans. Ultrason., Ferroelectr., Freq. Control*, vol. 49, no. 10, pp. 1363–1374, Oct. 2002.
[38] L. Tong, A. Ramalli, R. Jasaityte, P. Tortoli, and J. D'hooge, "Multi-transmit beam forming for fast cardiac imaging—Experimental validation and in vivo application," *IEEE Trans. Med. Imag.*, vol. 33, no. 6, pp. 1205–1219, Jun. 2014.
[39] F. Prieur, B. Dénarié, A. Austeng, and H. Torp, "Multi-line transmission in medical imaging using the second-harmonic signal," *IEEE Trans. Ultrason., Ferroelectr., Freq. Control*, vol. 60, no. 12, pp. 2682–2692, Dec. 2013.
[40] S. F. Nagueh *et al.*, "Recommendations for the evaluation of left ventricular diastolic function by echocardiography," *J Am. Soc. Echocardiogr.*, vol. 22, no. 2, pp. 107–133, 2009.
[41] V. Tavakoli, N. Bhatia, R. A. Longaker, M. F. Stoddard, and A. A. Amini, "Tissue doppler imaging optical flow (TDIOF): A combined B-mode and tissue doppler approach for cardiac motion estimation in echocardiographic images," *IEEE Trans. Biomed. Eng.*, vol. 61, no. 8, pp. 2264–2277, Aug. 2014.
[42] J. Poree, D. Garcia, B. Chayer, J. Ohayon, and G. Cloutier, "Non-invasive vascular elastography with plane strain incompressibility assumption using ultrafast coherent compound plane wave imaging," *IEEE Trans. Med. Imag.*, vol. 34, no. 12, pp. 2618–2631, Dec. 2015.
[43] C. Demene *et al.*, "Spatiotemporal clutter filtering of ultrafast ultrasound data highly increases doppler and fUltrasound sensitivity," *IEEE Trans. Med. Imag.*, vol. 34, no. 11, pp. 2271–2285, Nov. 2015.

Supplementary content — High-frame-rate echocardiography using coherent compounding with Doppler-based motion-compensation

Jonathan Porée, Daniel Posada, Amir Hodzic, François Tournoux, Guy Cloutier, Damien Garcia

A. Far-field acoustic pressure fields

We here derive the far-field acoustic pressure field generated by a uniform linear array in the frequency domain. In this study, we modeled a Philips / ATL P4-2 phased array probe (64 elements, central frequency = 2.5 MHz, fractional bandwidth at 6 dB = 60%, pitch = 0.3 mm, kerf = 50 μm). Each element acted as pistons whose normal velocity was described by a Tukey-shaped magnitude spectrum centered at 2.5 MHz. No apodization was considered and we assumed that the transducer elements were surrounded by a soft baffle. The acoustic pressure received by a scatterer located in the far-field of the array can be described in terms of its polar coordinate (r,θ) relative to the transducer center (origo of the x-z coordinate system, Fig. 1). In the frequency domain, the 2-D far-field pressure field generated by a 1-D uniform linear array is given by (see Eq. 4.14 p 77 in [28])

$$P(r,\theta,\omega,t) = \sum_{n=1}^{N} W_n e^{i\omega\Delta\tau_n}\left[\rho c v_0(\omega)\sqrt{\frac{2}{i\pi}}kb\, D_b(\theta,\omega)\frac{e^{ikr}}{\sqrt{kr}}e^{-ikx_n sin\theta}\right]e^{-i\omega t}, \quad \text{(S1)}$$

where $i=\sqrt{-1}$, t is time, ω is the angular frequency, ρ is the medium density and $k=\omega/c$ is the wavenumber. In this equation, it is assumed that the N individual elements act as pistons whose normal velocity in the frequency domain is $v_0(\omega)$. The weights W_n applied to these N elements represent the apodization values. Because no apodization was considered in our study, $W_n = 1, \forall n$. The frequency-dependent function $D_b(\theta,\omega)$ is the directivity function of an individual element of width $2b$ and is described later (Eq. S6). The delay laws $\Delta\tau_n$ for circular diverging beams are given by Eq. (2) of the main document and x_n $(n = 1 \ldots N)$ is the centroid location of the n^{th} element. By reorganizing Eq. (S1), the far-field pressure becomes

$$P(r,\theta,\omega,t) = \rho c v_0(\omega)\sqrt{\frac{2k}{ri\pi}}\, b\, D_b(\theta,\omega)e^{i(kr-\omega t)}\sum_{n=1}^{N} e^{i\omega\Delta\tau_n}\, e^{-ikx_n sin\theta}. \quad \text{(S2)}$$

In the (x,z) coordinate system represented in Fig. 1, the centroid locations of the individual elements are given by

$$x_n = \frac{2n-1-N}{2}p, \quad \text{(S3)}$$

where p is the pitch of the linear array. The far-field acoustic pressure (Eq. S2) can thus be rewritten as

$$P(r,\theta,\omega,t) = \rho c v_0(\omega)\sqrt{\frac{2k}{ri\pi}}\, b\, D_b(\theta,\omega)e^{i(kr-\omega t)}e^{ikp\frac{N-1}{2}sin\theta}\sum_{n=1}^{N}\left\{e^{i\omega\Delta\tau_n}\left(e^{-ikp\, sin\theta}\right)^{n-1}\right\}, \quad \text{(S4)}$$

Note that the last term represents a polynomial of degree (N-1) evaluated at $\left(e^{-ikp\, sin\theta}\right)$ and can be efficiently evaluated using the iterative Horner's method. Neglecting multiplicative constants, the amplitude of the acoustic pressure field in circular wave imaging reduces to

$$|P(r,\theta,k)| = \sqrt{\frac{k}{r}}|v_0(k)||D_b(\theta,k)|\left|\sum_{n=1}^{N}\left\{e^{ik\sqrt{(x_n-x_v)^2+z_v{}^2}}\left(e^{-ikp\, sin\theta}\right)^{n-1}\right\}\right|. \quad \text{(S5)}$$

We recall that $D_b(\theta)$ represents the angular response of a single element in the far-field. It was assumed that the transducer elements were surrounded by a soft baffle, so that

$$D_b(\theta,k) = cos\theta\,\frac{sin(kb\, sin\theta)}{kb\, sin\theta}. \quad \text{(S6)}$$

To analyze the radiation patterns, we estimated the root-mean-squared (RMS) acoustic pressure using equations (S5) and (S6):

$$P_{\text{RMS}}(\theta) = \sqrt{\int_k |P(r,\theta,k)|^2\, \mathrm{d}k}. \quad \text{(S7)}$$

If coherent summation of M diverging-beam-based acoustic pressure fields is performed at an angle θ_c, the amplitude of the resulting compound pressure far-field can be derived from Eq. S5:

$$|P_c(r,\theta,k)| = \sqrt{\frac{k}{r}}|v_0(k)||D_b(\theta,k)|\left|\sum_{m=1,n=1}^{M,N}\left\{e^{ik\sqrt{(x_n-x_{v_m})^2+z_{v_m}{}^2}}\left(e^{-ikp\,(sin\theta-sin\theta_c)}\right)^{n-1}\right\}\right|. \quad \text{(S8)}$$

The new term ($e^{ikp\,sin\theta_c}$) in the array factor corrects phases when compounding response is steered towards θ_c; *i.e.* the weights in Eq. S1 are written as $W_n = e^{ikx_n sin\theta_c}$ to perform beam steering. The (x_{v_m}, z_{v_m}) represent the coordinates of the M virtual sources.

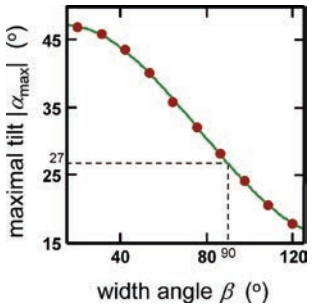

Fig. S1 – *Directivity analysis.* For a given width angle (β), too large tilting may induce significant grating lobes (see Fig. 1, right panel). To obtain adequate directivities when emitting circular beams, we sought the maximal acceptable tilts using numerical simulations in the far-field. This figure represents the maximal tilt as a function of the width angle. For a 90°-wide sector, tilt angles (α) larger than 27° (absolute value) should be avoided. In this study, we used $|\alpha| \leq 25°$. The dots represent the simulation results; the curve is a fitting.

B. Tilt angles

To obtain high-quality cardiac images, we coherently combined several complex envelope (IQ, in-phase and quadrature) signals steered at different linearly distributed angles. It is critical to use tilt angles as large as possible to get a large virtual aperture and thus better lateral resolution. However, as illustrated by Fig. 1, large tilted angles can lead to detrimental transmit grating lobes. We thus determined which tilts can be acceptable for the P4-2 phased array probe. This allowed us to pick out the *in vitro* and *in vivo* compounding transmit sequences for a given sector of interest. For this purpose, we defined the following directivity parameter:

$$dir(\alpha,\beta) = \frac{\int_{\alpha-\beta/2}^{\alpha+\beta/2} P_{\mathrm{RMS}}^2(\theta)\mathrm{d}\theta}{\int_{-\pi/2}^{\pi/2} P_{\mathrm{RMS}}^2(\theta)\mathrm{d}\theta}. \quad \text{(S9)}$$

where P_{RMS} is the root-mean-square (RMS) acoustic pressure in the far-field. The insonified area is expected to be included in the region delimited by the angles $(\alpha - \beta/2, \alpha + \beta/2)$ (see Fig. 1 of the main document). The numerator of Eq. (S9) represents the energy in this expected insonification area. The directivity parameter given by Eq. (S9) thus characterizes the amount of acoustic energy present in the expected zone; a value of 1 reveals an "optimal" directivity. For example, directivity parameters associated to the radiation patterns of Fig. 1 of the main document, $(\alpha = 0°, \beta = 90°)$, $(\alpha = 30°, \beta = 90°)$, are $dir(0°, 90°) = 0.97$ and $dir(30°, 90°) = 0.83$, respectively. For a given width angle β, the maximal acceptable (in terms of directivity) tilt α_{max} was determined from

$$\frac{dir(|\alpha_{max}|,\beta)}{dir(0,\beta)} = 90\%. \quad \text{(S10)}$$

Equation (S10) indicates a similarity of 90% in term of directivity between non-tilted and tilted angles. The maximal tilt angle $|\alpha_{max}|$ based on this criterion decreases with increasing width angle β (Fig. S1). For a 90°-wide sector, the maximal "acceptable" tilt for the P4-2 probe was estimated at 27° (Fig. S1). Directivity at 30° for a 90°-wide sector is thus suboptimal (Fig. 1 of the main document, bottom right) according to our criterion. Based on this rule of thumb, we used 25° as maximal absolute value of the tilt angle (*i.e.* $|\alpha| \leq 25°$).

C. Transmit sequences for coherent compounding

To carry out coherent compounding, we recall that only the tilt (α) was changed. The tilt angles α_m were linearly spaced between -25° and +25°. According to Fig. S1, and as explained in the previous section, such α values ensured good transmit directivity for width angles smaller than 90°. For each (α_m, β), the corresponding virtual sources (x_{v_m}, z_{v_m}) and transmit delays were given by equations (1) and (2). These uniformly spaced tilt angles were ordered in a specific manner (a "triangle" sequence) to optimize motion estimation and motion compensation, as detailed in paragraph II.B.4 "*The triangle sequence: justification*" of the main document. We also determined a suitable number of transmits as now clarified.

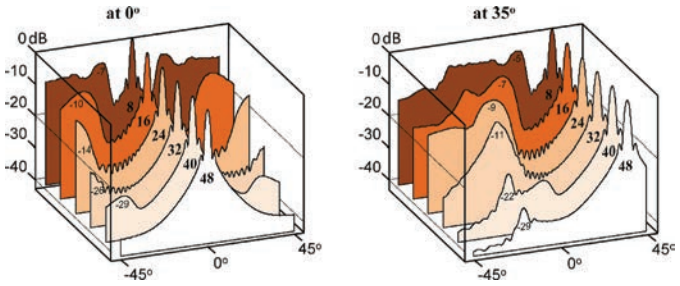

Fig. S2 – *Compound acoustic fields.* Compound far-field radiation patterns (RMS acoustic pressure fields) were simulated for a 60% bandwidth 2.5 MHz 64-element phased-array. The sector of interest was 90°-wide. A number of 8 to 48 90°-wide tilted circular beams were generated. Coherent compounding was simulated at 0° (left panel) and 35° (right panel). According to these simulations, transmit of 32 circular beams is a good option to minimize the compound sidelobes in a 90°-wide sector.

Since no transmit focusing was performed, coherent compounding of several individual complex envelopes (*i.e.* IQ images) was necessary to produce high-contrast ultrasound images. Using numerical simulations in the far-field, we sought the number of transmits (M) that offered a good compromise between image quality and frame rate. Since the 90°-wide sector is commonly used in ultrasound cardiac imaging, we focused on this configuration in this numerical study. It also represents the worst-case scenario if we are interested in width angles smaller than 90°. If coherent summation of M diverging-beam-based acoustic pressure fields is performed at a given angle θ_c, the amplitude of the resulting compound pressure far-field is given by Eq. S8. Using the abovementioned transducer properties (see II.A), we simulated 90°-wide

RMS pressure far-fields (Eq. S6-8) compounded at $\theta_c = 0^o$ and 35^o, and generated from M = 8, 16, ... or 48 diverging circular beams. As previously mentioned, the tilt angles α_m were linearly spaced between -25° and +25°. Our simulations expectedly showed that grating lobe intensity decreased with increasing compounding number M (Fig. S2). Grating lobes were more significant when compounding response was steered towards 35° in comparison with 0°. Based on these simulations, we selected M = 32 for the *in vitro* and *in vivo* experiments. With such a compounding number, we should expect grating lobe levels smaller than -10 dB.

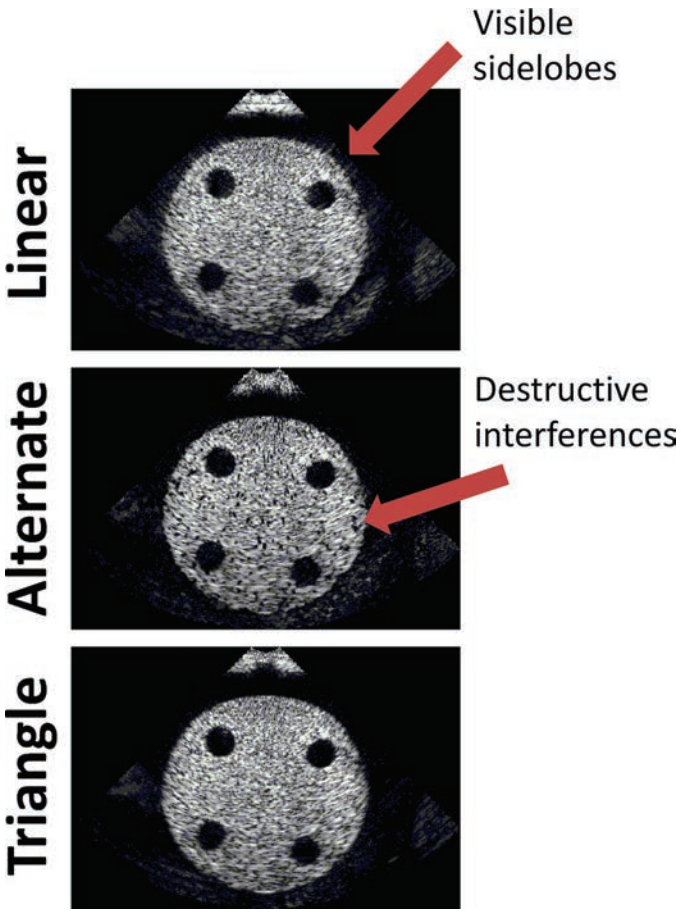

Fig. S3 – *Close-up of Figure 7*. This figure highlights the artifacts generated by the linear and alternate sequences. Sidelobes and destructive interferences are not present with the triangle sequence.